Chapter 3
Kitchen Physics: Neutral Density and Ion Temperature Measurements

3.0 Introduction

In addition to the direct measurements of the plasma potentials and flows, there are further measurements which are necessary to understand the damping of plasma flows. Knowledge of the neutral density is necessary for the determination of the ion-neutral friction, while the ion temperature is necessary for the determination of the ion collisionality regime and the ion pressure in the calculation of the viscosity. Both the neutral density and the ion temperature are determined by spectroscopic measurements in HSX.

The H_α based neutral density measurement is described in Section 1. This discussion includes a description of the detectors, the method of absolutely calibrating the system, and a brief description of the data analysis methods. The Doppler spectroscopy system for measurement of the ion temperature is discussed in Section 2. The collisional coupling between electrons, majority protons, and impurity ions is the subject of Section 3. The ion collisionality regime for HSX is briefly discussed in Section 4.

This spectrometer system is also capable of making impurity flow measurements. The details of making these measurements and some preliminary results are discussed in Appendix 4.

3.1 Neutral Density Measurements in HSX.

The neutral density measurement in HSX is made using a set of H_α detectors distributed around the torus. There are two arrays of absolutely calibrated H_α detectors, configured to allow monitoring of hydrogen fueling from both the walls and the gas puff. The design, calibration, and use of the detectors are detailed in the following sections.

3.1.1 Description of H_α Detectors

The H_α detector system is composed of 15 detectors. Nine of these detectors are placed at a single vertical plane at the location of the gas puff in a "poloidal array", as illustrated in figure 3.1. The six other detectors are placed toroidally around the machine. Figure 3.2 shows the distribution of the detectors on the torus, as well as the gas puff location.

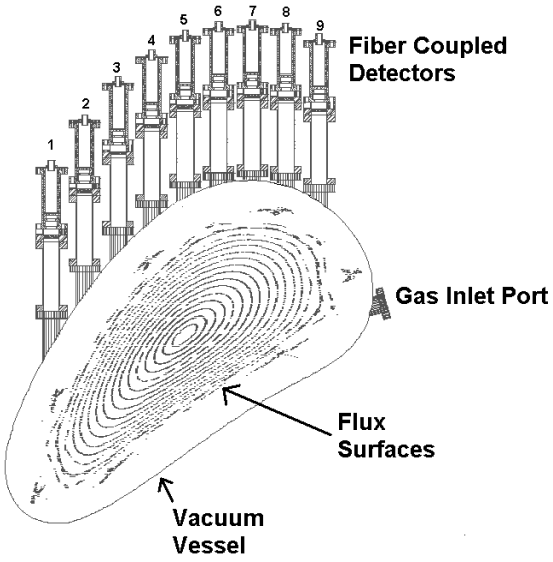

Figure 3.1: Poloidal array of collection optics for H_α detectors.

Each detector is composed of two parts: a collection optics assembly shown in figure 3.3 and a detector/amplifier assembly. Light from the plasma exits HSX though a .6" diameter clear aperture window at the end of a 3" long mini-conflat double nipple. This long extension tube prevents the glow discharge from applying a coating to the window, which would destroy the transparency. The collection optics themselves are composed of an H_α interference filter followed by a plano-concave lens. An SMA connected fiber optic is placed at the focal point of the lens. The entire system is designed so that the acceptance cone of light does not intersect the double nipple or vessel wall at the entrance to the vessel, as illustrated by the rays in the figure. This

feature was tested in the calibration process and confirmed to be true. Hence, no extra calibration step is required to account for the different lengths of tubulation on the miniflange arrays. There are no view dumps currently in the system.

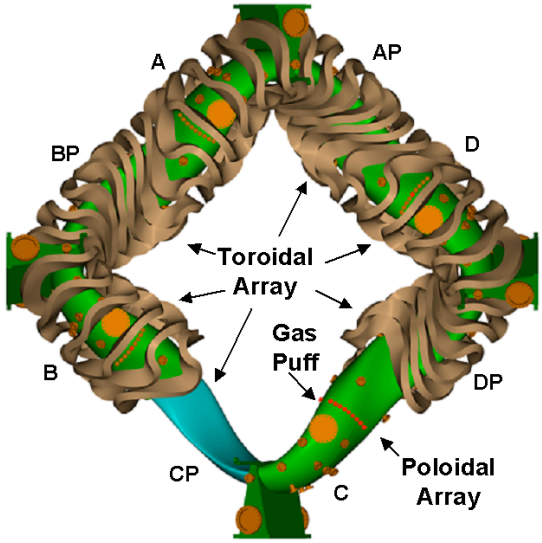

Figure 3.2: Distributions of H_α detectors around HSX, as well as the gas puff location and the labels of the various field periods.

The detector and amplifier are placed in a single aluminum box, one box per spatial channel. An SMA fiber coupler is mounted on the outside of the box, holding the fiber so that its light shines on the face of the detector. This detector consists of a photodiode and an op-amp inside the same package, eliminating the need for an external transimpedance stage. The internal op-amp circuit is configured for a transimpedance of 10^8 Ω, and a bandwidth of 2kHz. The signal from the detector is run through a second gain stage; the gain in this stage has been set by the light levels at the various viewing locations, but generally is in the range of 3 V/V to 30 V/V. The signals from all 16 channels are digitized on the same digitizer at 10 kHz. A complete list of parts for the system can be found in Appendix 1, as well as detailed drawings of all the components.

The original design for these detectors had the amplifier mounted directly to the collection optics on HSX. This design had the advantage of simplicity, but suffered from mysterious "spikes" in the signal. Much testing revealed that these spikes were present even when the light was blocked,

and for any combination of grounding configurations. Eventually, it was discovered that placing lead shielding around the detector prevented the spikes, implying X-ray contamination of the signal. Since it is impossible to place lead shielding directly in the light path, it was necessary to switch to a fiber-coupled design and house the amplifiers behind lead sheet. This has proven to be a generally satisfactory solution to the problem, although X-ray contamination can occur for very low density discharges with large X-ray fluxes.

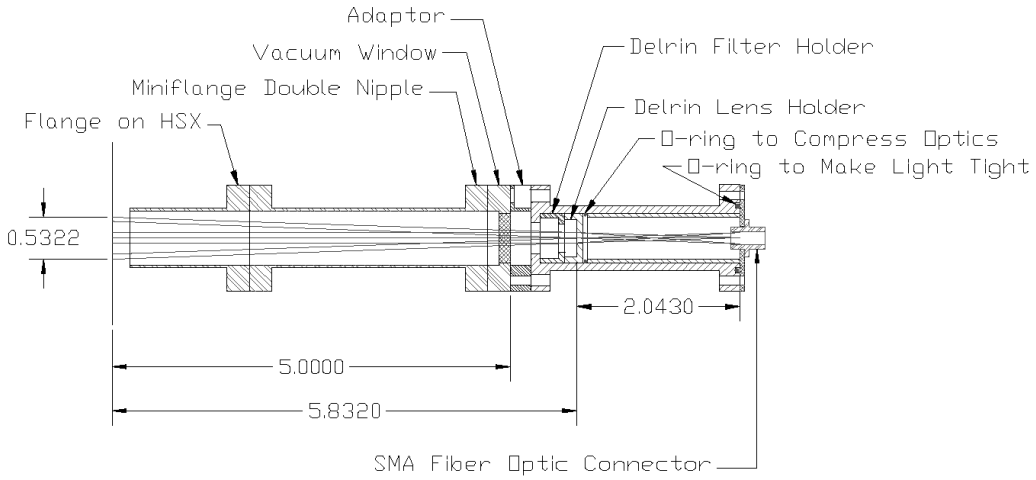

Figure 3.3: Schematic of the H_α detector.

3.1.2 Absolute Calibration of the H_α detectors.

For the H_α diagnostic to provide useful data, the system must be absolutely calibrated. The procedure of completing this calibration has been detailed by J. K. Anderson.[1] The description below describes this process as it has been applied to the H_α diagnostic on HSX.

The voltage measured by an optical detector is given by

$$V_{measured} = kT \int_0^\infty \int_0^L \int_{dA} f(\lambda)\varepsilon(\lambda,l)\Delta\Omega(l)\,dA\,dl\,d\lambda . \qquad (3.1)$$

Here, k is a constant relating the power on the detector to the output voltage with units of V/W. $\varepsilon(\lambda,l)$ represents the emissivity of the plasma as a function of wavelength and length along the viewing chord, and has units of W/(cm^3·nm·sr). The solid angle of light collected at each point along the chord is $\Delta\Omega$ and is measured in steradians, dA represents the perpendicular area of the viewing chord along the chord, dl represents the length increment along the chord, T is a constant representing the (wavelength independent) losses of power in any components of the optical system, and $d\lambda$ represents the contribution of each wavelength to the total power detected. The unitless wavelength dependent sensitivity of the detection system is $f(\lambda)$, and is determined in this case by the interference filter. The typical wavelength response of the H_α filter used in HSX is shown in figure 3.4 as measured by the 1 meter spectrometer described in the next section. All filters used in the H_α arrays on HSX had their transfer function measured in this way. A hydrogen discharge lamp[2] is used to identify the exact location of the H_α line in the figure.

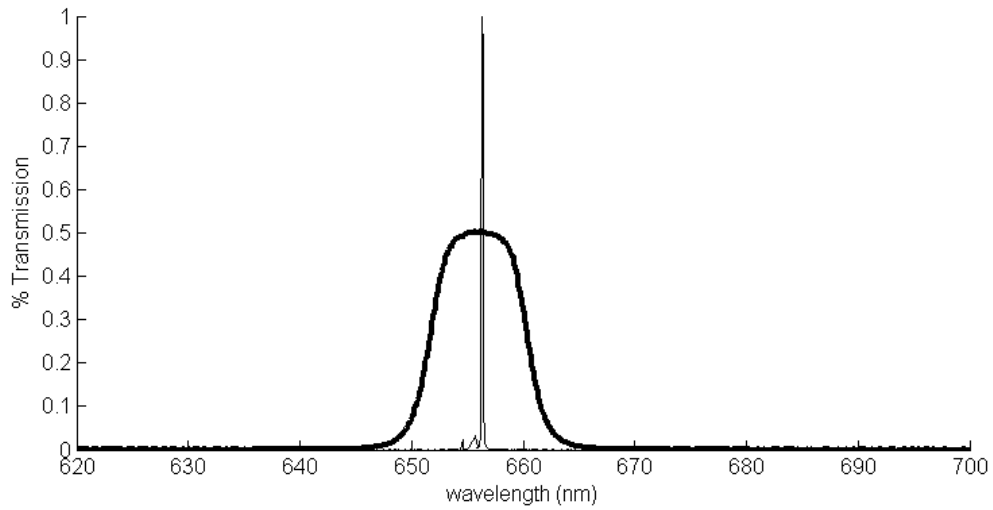

Figure 3.4: Example Filter Transfer Function and H_α line.

Assume that the emissivity varies along, but not across, the viewing chord. Elements at each area along the chord contribute equally to the signal, so that

$$\iint_{A(l)} \Delta\Omega(l)\,dA = A\Delta\Omega \tag{3.2}$$

is a constant. With this assumption, the measured voltage can be written as

$$V_{measured} = kTA\Delta\Omega \int_0^{\infty}\int_0^{L} f(\lambda)\varepsilon(\lambda,l)\,dl\,d\lambda . \tag{3.3}$$

To continue, we use an integrating sphere white light calibration source.[3] The integrating sphere has an emissivity of the form $\varepsilon(\lambda,l)=R(\lambda)\delta(l-r_{sphere})$, where R is the spectral radiance of the output port of the sphere in units of $W/(cm^2 \cdot nm \cdot sr)$. The spectral radiance has been measured by the manufacturer at discrete wavelengths. We have fit the spectral radiance to a blackbody of the form

$$f_{BB}(\lambda) = \frac{hc^2}{2\pi\lambda^5\left(e^{hc/\lambda kT}-1\right)}. \tag{3.4}$$

Figure 3.5 shows the measured spectral radiance, along with the fit for a temperature of 3040 K.

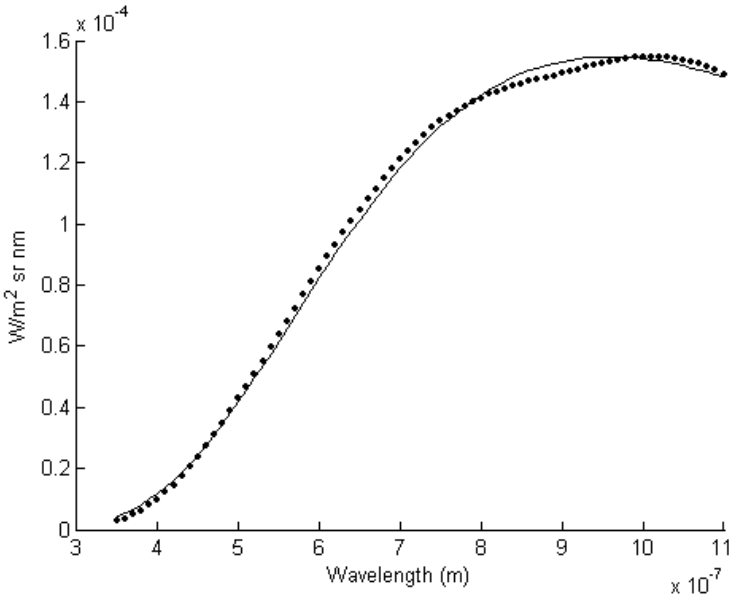

Figure 3.5: Spectral Radiance of the Integrating Sphere Light Source

Using the form of the emissivity given above for the integrating sphere, the voltage output when the detector faces the sphere can be expressed as

$$V_{sphere} = kA\Delta\Omega T\int_0^{\infty}\int_0^{L} f(\lambda)\delta(l - r_{sphere})R(\lambda)\,dl\,d\lambda. \quad (3.5)$$

The integral along the viewing chord can be performed trivially to yield

$$V_{sphere} = kAT\Delta\Omega\int_0^{\infty} f(\lambda)R(\lambda)\,d\lambda'. \quad (3.6)$$

Hence, the desired quantity $k'=kAT\Delta\Omega$ can be calculate as simply $k'=V_{sphere}/R'$, where R' is defined as

$$R' = \int_0^{\infty} f(\lambda)R(\lambda)\,d\lambda. \quad (3.7)$$

With these expressions, V_{sphere} is a measured quantity, and R' can be calculated from the known filter transfer function and sphere spectral radiance. The quantity k' is thus solved for.

When making actual measurements of the H_α spectral line, it is necessary to account for the fact that the spectral line does not fill the entire band pass of the filter. In particular, the emissivity of the H_α line can be represented as $\varepsilon_{H\alpha}(\lambda,l)=I_{H\alpha}(l)\delta(\lambda-\lambda_{H\alpha})$, where the intensity $I_{H\alpha}(l)$ has units of $W/(cm^3 sr)$. The measured voltage from line integrated H_α emission can then be written as

$$V_{H\alpha} = k'\int_0^{\infty}\int_0^{L} f(\lambda)\varepsilon_{H\alpha}(\lambda,l)\,dl\,d\lambda. \quad (3.8)$$

The integration over wavelength is trivial and leads to

$$V_{H\alpha} = k' f(\lambda_{H\alpha})\int_0^{L} I_{H\alpha}(l)\,dl. \quad (3.9)$$

Having determined all of the calibration factors, the line integrated intensity can now be calculated as

$$\int_0^{L} I_{H\alpha}(l)\,dl = V_{H\alpha} / k' f(\lambda_{H\alpha}). \quad (3.10)$$

This line integrated intensity is the physics quantity to be used to infer the distribution of neutrals in HSX.

3.1.3 Example Data from the H_α System

An example of the H_α signals from the toroidal array is shown in figure 3.6, for a discharge with six pulses of the bias electrode. The detector in field period C directly views the gas inlet, and always has a much larger signal than the other detectors. The detector in field period DP views some recycling off of the biased electrode. Note that the other detectors have had their signal multiplied by 10 in this graph so that they are all visible on the same scale. The behavior of the H_α signal during the electrode pulse will be discussed in more detail in Section 4.3.

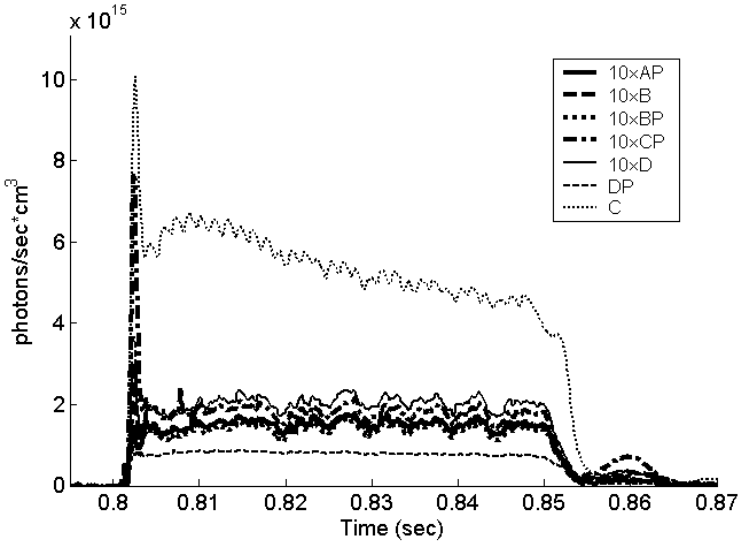

Figure 3.6: Example time traces from the H_α system.

3.1.4 Interpretation of the Results Using the DEGAS code.

There are a number of factors which make it difficult to infer the density of molecular and atomic hydrogen from the simple H_α measurements. Two of the more egregious difficulties are:

1: The H_α emission is not a flux surface function, making it very difficult to invert the emission distribution without having many (possibly hundreds of) detectors.

2: Both atomic hydrogen and dissociating hydrogen molecules contribute to the H_α emission. It is difficult to separate out the contribution from these two sources without some independent knowledge of their densities.

To resolve these problems, the DEGAS[4] code has been used by John Canik to model the three dimensional distribution of neutrals in HSX, using the measured electron density profile[5] and H_α emission to constrain the simulations. In this code, the three dimensional plasma density and temperature distributions are provided as inputs, and are fixed in time. The location and source rate of neutral gas is provided by the user. Using Monte Carlo techniques, flights of neutral particles are launched from the puff locations. The flights are followed as collisions ionize the neutral particles; the code stops monitoring the flight when a sufficient number of the neutrals in the flight have been ionized so that the flight is no longer numerically significant. Charge exchange and wall reflections of the neutrals are included in the simulation. The locations where ionization occurs gives the source rate, which can be related to the neutral density. This neutral density, along with the electron temperature and density profiles, is then used to calculate H_α emission and the signal that would be collected along chords through the plasma.

In the HSX modeling,[6] the source is considered to consist of both wall recycling and gas puffing. The recycling source is modeled by scaling the DEGAS wall source until the signals in the toroidal array of H_α detectors far from the puff match the simulated H_α emission along those chords. The gas puff source in DEGAS is then scaled so that the simulated H_α emission at the center chord of the poloidal array matches the measured emission. An example of the agreement between the measured chordal H_α emission and the DEGAS prediction for the poloidal array is shown in figure 3.7. Recall that gas is entering the plot from the left of the figure 3.7, as indicated in figure 3.1. This figure illustrates the excellent agreement between the measurements and the modeling. More data regarding the neutral distribution in HSX will be shown in Section 6.3.

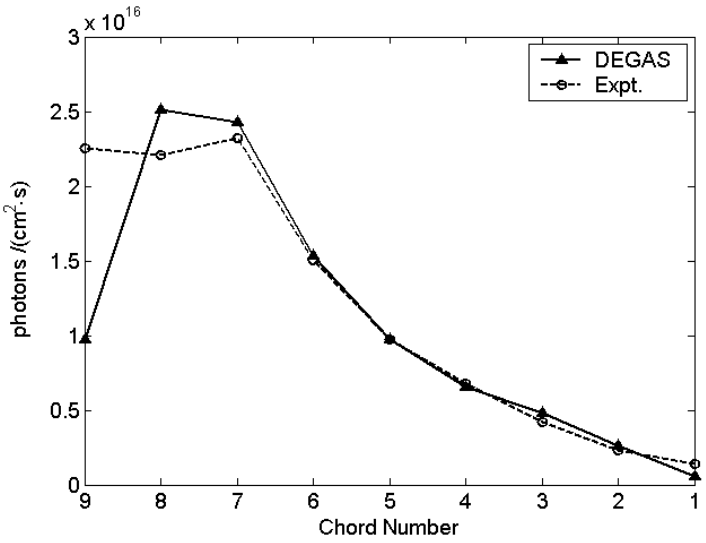

Figure 3.7: Comparison between the measured and modeled signals at the poloidal array of H_α detectors. DEGAS calculations and figure by John Canik.

3.2: Measurements of Impurity Ion Temperatures in HSX.

Impurity ion temperatures are measured in HSX using Doppler spectroscopy. In this technique, the broadening in wavelength of a spectral line is used to estimate the temperature of the species which emitted the spectral line. More information on this technique can be found in the references, particularly the book by Thorne et al.[7] This section describes the measurements made on HSX and provides some results.

3.2.1: Description of the Measurement System

To implement this measurement, it is necessary to have a spectrometer with sufficient dispersion and optical throughput to accurately measure the spectral distribution of light from the plasma. The parameters of the one-meter spectrometer used on HSX are given in table 3.1.

Focal Length	1meter
f/#	8
Spectrometer Configuration	Czerny-Turner
Ebert Angle	5.3°
Grating Size	10cm x 10cm
Useful Wavelength	200-500 nm for 3600 g/mm grating 200-~1000nm for 300 g/mm grating
Entrance Slit	Micrometer driven jaws, fast shutter
Detector	LN_2 cooled, back thinned CCD
CCD Pixel Size	26μ x 26μ
Exposures per Discharge	1
Control	Grating, Shutter, and CCD controlled by LabVIEW

Table 3.1: Specifications of the 1meter spectrometer system

Light is coupled to the instrument through a trifurcated fiber bundle; three individual large core diameter fibers are brought into a ferrule, where they are arrayed in a vertical line. This line of three fibers is placed at the entrance slit of the spectrometer and is imaged on the CCD; the columns of the CCD operate as the effective exit slit of the instrument. The specifications of optical fiber can be found in Appendix 1.

There are currently three different collection optics schemes for coupling light from HSX to the spectrometer. For making profiles of emission, a 9 chord array has been constructed on the mini-flange array on field period A. The geometry of this array is identical to that of the H_α shown in figure 3.1. The presence of this array is the reason that the toroidal array of H_α detectors does not have a detector on this half field period. These 9 chords suffer from a restricted light level due to the small size of the flanges (the inner diameter of the mini-flange weld stubs on HSX is 0.68"). A single collection optics assembly capable of holding all three fibers has also been installed on HSX. This assembly views HSX through a 2 ¾" diameter conflat window (1.4" clear aperture), and is able to collect more light than the miniflange array optics. This view is more convenient when using the spectrum for spectral line surveys. The third viewing scheme uses a miniflange nipple welded into an 8" conflat flange at an angle such that an approximately toroidal view is possible when the assembly is placed on the 8" flange between coils 3 and 4. The data presented later in this chapter was taken using the miniflange collection optics array. All views utilize fused

silica windows and lenses to maximize the transmission of light in the 200-300 nm wavelength range.

The CCD suffers from the same problem of X-ray contamination as the H_α detectors, especially in low density discharges. The contamination appears as one or two pixel wide spikes on the CCD readout; they are easily identifiable as they are narrower than the instrument width for the slit widths in use during data taking. It has been found necessary to surround the CCD with lead bricks 2" thick. This is sufficient to eliminate most, but not all, of the X-ray contamination.

3.2.2: The Determination of the Dispersion and Instrument Function

When monochromatic light illuminates the entrance slit of the spectrometer, the entrance slit appears as a single image on the CCD. The dispersion of the instrument reveals how much the image of the entrance slit will move at the exit plane as the wavelength of the input light is changed. It can be calculated based on the physical properties of the spectrometer and the wavelength of light being studied. Define 'a' to be the distance between grooves on the grating, k the grating order being used, λ the wavelength of light, φ the Ebert angle of the spectrometer, and f the focal length. The dispersion is then given by

$$D = \frac{dx}{d\lambda} = \frac{fk}{a\cos\left(\sin^{-1}\left(\frac{k\lambda}{2a\cos(\varphi)}\right) - \varphi\right)}(\mu/nm). \qquad (3.11)$$

For the instrument used on HSX, k=1, f=1 meter, φ=5.3°, and 'a' is 1/3600 mm^{-1} or 1/300 mm^{-1}, depending on the grating installed in the instrument.

The dispersion can be determined by measuring the spatial separation (at the exit plane) between closely spaced spectral lines. This has been done using spectral lines from a mercury pen lamp, with the results shown in figure 3.8. The dispersion determined from the equation (3.11) appears to agree well with the data.

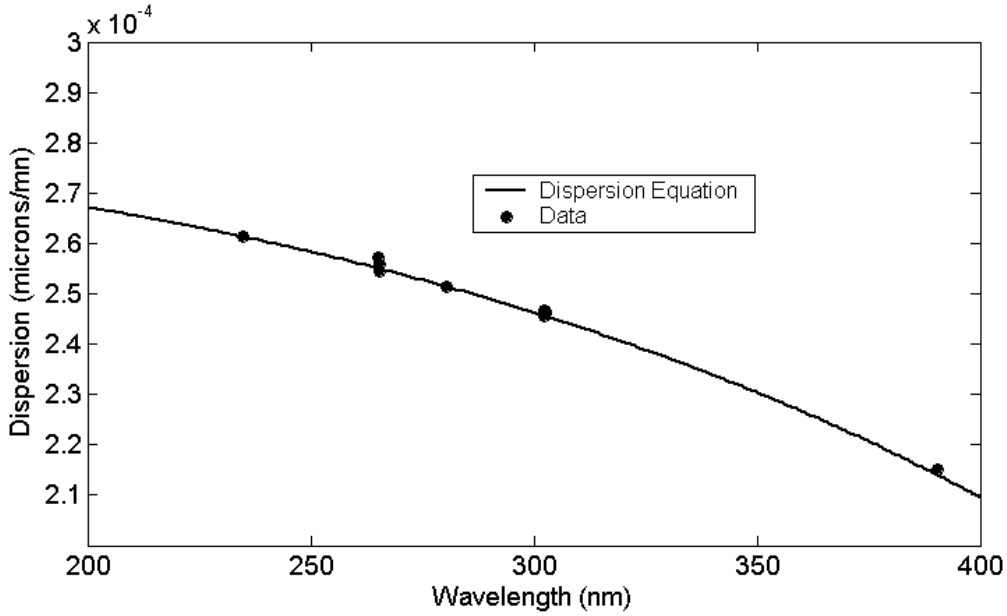

Figure 3.8: Measurements of the dispersion and the curve specified by equation (3.11).

When light from a narrow (in wavelength) spectral line is input to the spectrometer, the line will have finite width at the exit plane due to instrument broadening. This artificial broadening of the spectral line can lead to an overestimation of the ion temperature if not properly accounted for. The spatial width of the spectral line at the exit plane is determined by the width of the entrance slit, which is in turn determined by a micrometer drive. The Hg line at 265.2 nm was fed through the fibers and imaged onto the CCD. The image of the line was fit to a Gaussian function,

$$f(\lambda) = \exp\left(\frac{(p - p_o)^2}{2w_i^2}\right), \tag{3.12}$$

for a series of different slit widths, enabling the instrument width w_i to be measured. The result is shown in figure 3.9. For larger entrance slit widths, w_i is linearly dependent on the entrance slit. At small entrance slit widths, w_i tends towards a constant of approximately .75 pixels, representing the minimum image width.

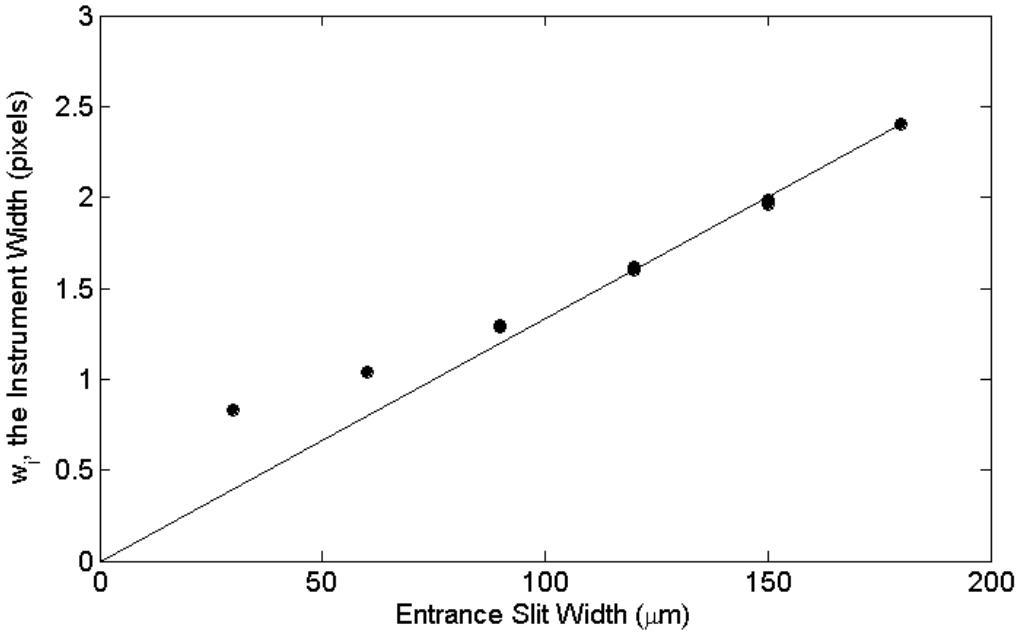

Figure 3.9: Instrument width as a function of entrance slit width.

Similar measurements have been made at fixed entrance slit width, but for different spectral lines. These measurements showed that the instrument function is largely independent of wavelength in the range of interest.

3.2.3: Ion Temperature Measurements.

The spectral lines in the emission spectrum of HSX are generally fit to a function of the form

$$f(p) = B + C\lambda + \sum_{k=1}^{n} A_k \exp\left(\frac{(p - p_k)^2}{2w_k^2}\right). \tag{3.13}$$

In this expression, p represents the pixel number, p_k is the center of the k^{th} spectral line; w_k is the spectral line width measured in pixels. The factors B and C allow some offset to the data, and the sum is over overlapping spectral lines. For the spectral lines studied in HSX to date, there are at most two overlapping spectral lines (the C^{4+} lines as 227.727nm and 227.792nm). An example of the fit is provided in figure 3.10, for the C^{4+} line at 227.089 nm, where the data, the Gaussian fit,

and the Gaussian instrument function are shown. The instrument broadening contributes most of the measured line width.

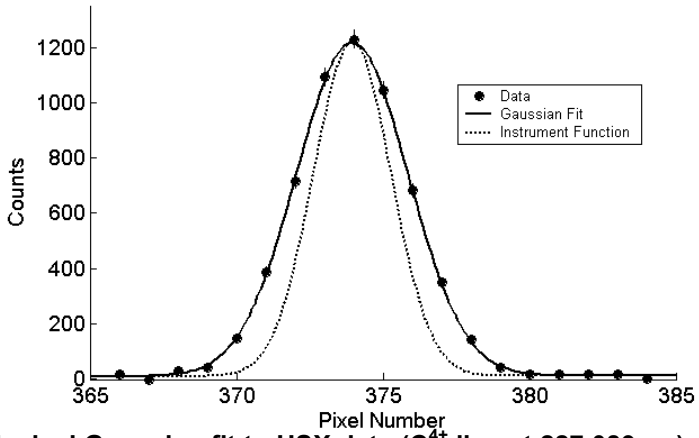

Figure 3.10: Typical Gaussian fit to HSX data (C^{4+} line at 227.089nm), as well as the instrument function.

It can be shown that for a Doppler broadened spectral line with Gaussian shape as in (3.13), the ion temperature from the k^{th} spectral line is given by[8]

$$T_k = \left(\frac{\partial \lambda_k}{\lambda_{o,k}} \right)^2 m_k c^2 . \qquad (3.14)$$

In this expression, $\lambda_{o,k}$ is the rest wavelength of the k^{th} spectral line, $\delta\lambda_k = a w_k / D$ is the width parameter in the Gaussian fit (in nanometers), and m_k is the mass of the ion emitting the light.

As noted above, the spectrometer itself causes broadening of the spectral lines. Approximating the instrument function by a Gaussian, and using the fact that the convolution of two Gaussians is another Gaussian, the correction for the instrument broadening can be easily approximated in the temperature formula by writing[8]

$$w_k \rightarrow \sqrt{w_k^2 - w_i^2} .$$

The Gaussian fit is calculated in terms of pixels, not wavelength. Hence, it is more appropriate to write the ion temperature from the k^{th} spectral line as

$$T_k = \left(\frac{\sqrt{w_k^2 - w_i^2}\, ac}{\lambda_{o,k} D} \right)^2 m_k . \qquad (3.15)$$

The dispersion and the instrument width of the spectrometer are not perfectly well known, and there is some error in the fit parameters. It is possible to do standard error propagation analysis[9] on this expression to calculate uncertainties in T_i based upon uncertainties in the line width, instrument width, and dispersion. The uncertainty on the line width is calculated during the fit of expression 3.13. The uncertainty in the instrument width is estimated by repeated measurements of the instrument width, and the uncertainty in the dispersion is estimated from the variation in the measured dispersion. The resulting error in the temperature is

$$\sigma_{T_k}^2 = \left(2\frac{m_k a^2 c^2}{\lambda_{o,k}^2 D^2} \right)^2 \left(w_k^2 \sigma_{w_k}^2 + w_i^2 \sigma_{w_i}^2 \right) + \left(2\frac{\left(w_k^2 - w_i^2 \right) a^2 c^2}{\lambda_{o,k}^2 D^3} m_k \right)^2 \sigma_D^2 . \qquad (3.16)$$

This expression is used to calculate the error bars in the ion temperature measurements discussed below.

3.2.4: Impurity Brightness and Temperature Measurements on HSX.

Doppler spectroscopy in HSX has been performed on ionized states of carbon and oxygen. Table 3.2 lists the spectral lines used for the measurements. The measurements of oxygen emission can be made in almost all discharges in HSX; the carbon lines require substantial methane doping of the plasma (~40% of the pressure in the gas system from CH_4) to achieve useful levels of light. The differences in ionization potential of the various states are important, as they allow some spatial localization of the signal: atomic states with higher ionization potentials will presumably be located farther inside the plasma, where the electron temperature is higher. Atomic physics modeling and inverted emission profiles necessary to localize the emission shells have not been done for HSX.

Element	Ionization State	Ionization Potential (eV)	Wavelength (nm)
Carbon	+4	392	227.089
Carbon	+2	47.9	229.690
Oxygen	+4	114	278.101
Oxygen	+4	114	278.699
Oxygen	+1	35.1	278.993

Table 3.2: Spectral Lines for Doppler Spectroscopy in HSX.

Note that the Doppler spectroscopy measurement requires that the 3600 g/mm grating be used. The dispersion of this grating is such that approximately 7nm of wavelength space can be imaged on the grating. This is sufficient to view either all of the oxygen lines in table 3.2, or all of the carbon lines. Hence, more than one ion temperature measurement can be made in a single discharge.

The impurity ion temperature and brightness have been measured as a function of line average density, in discharges doped with carbon and in undoped discharges, where residual oxygen was used for the measurement. The CCD integrated light for the final 35 msec. of the 50 msec. discharges, and only discharges which were stationary during this entire period are included in the analysis.

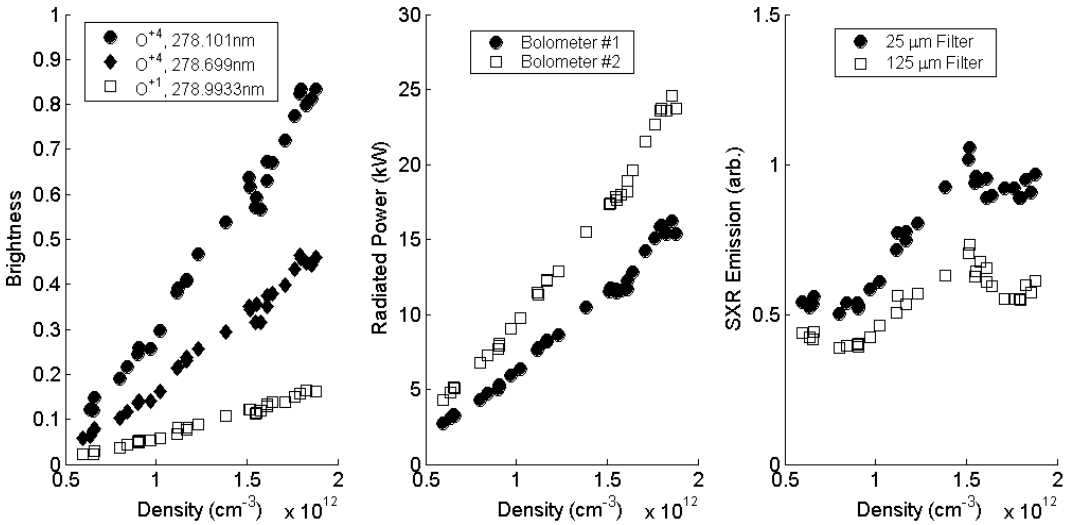

Figure 3.11: Oxygen brightness (left), radiated power (center) and soft X-ray emission (right) vs. line average density.

Only the oxygen experiments will be considered in this section, as they are most typical of the biased electrode discharges. The temperature and brightness of oxygen were measured on

a chord passing through the magnetic axis, while the density was scanned via gas puffing in standard QHS discharges. The result is shown in figure 3.11. The oxygen radiation tracks the radiated power. On the other hand, the soft X-ray emission has a very different trend and does not appear to be related as closely to the radiated power.

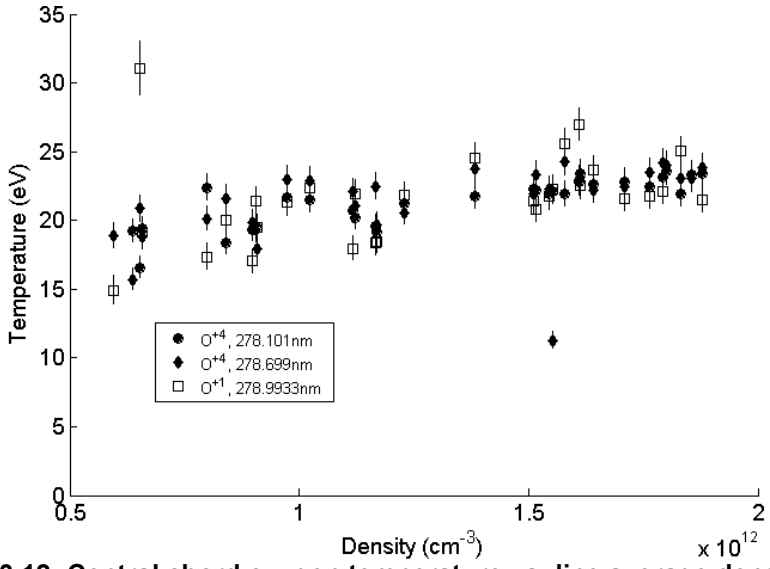

Figure 3.12: Central chord oxygen temperature vs. line average density, in the QHS configuration.

The ion temperature scaling for these two species is shown in figure 3.12. Two important trends should be noticed in this data. First, there is a slight rise in impurity ion temperature as the density rises. Secondly, the two O^{+4} temperature measurements are essentially the same as the O^{+1} temperatures, indicating that the ion temperature gradient is fairly small, at least in the region between where these species radiate.

Similar measurements were done in the Mirror configuration. The relationship between the oxygen brightness and radiated power is very similar to that in figure 3.11. The oxygen temperature is shown versus line average density in figure 3.13. The trend of a small ion temperature increase with density is apparent in this data as well, as is the similarity in the temperature between the two different species.

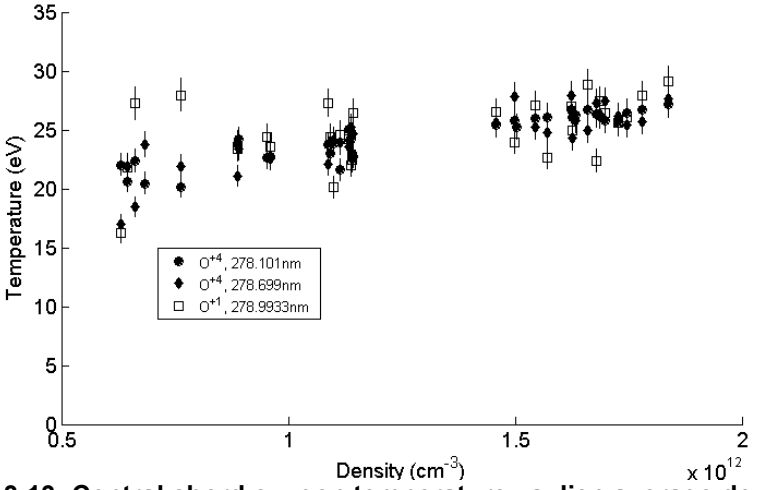

Figure 3.13: Central chord oxygen temperature vs. lien average density, in the Mirror configuration.

These density scanning experiments have also been conducted with substantial CH_4 doping, allowing the carbon lines to be studied. As with the oxygen profiles, the data indicates a small rise in the carbon impurity temperature as the density is raised, and essentially no difference in the temperature between the $C^{+2}$and C^{+4} ionization states. It should be noted that in discharges with substantial methane doping, there is steady accumulation of carbon in the plasma as the day progresses. It is not possible to maintain a steady brightness of carbon light for this reason. Hence, creating a reliable profile of the C^{+4} emission on a shot to shot basis using the miniflange collection optics array is quite difficult. In apparently identical undoped discharges, there is also some shot to shot variation in the O^{+4} brightness, probably due to the difference in recycling for different discharges.

3.3: Modeling of Electron/Proton/Impurity Coupling in HSX.

The data presented in the previous section are impurity ion temperatures. A natural question is to ask how this temperature relates to the proton temperature. It is also natural to ask if the neutral densities we measure are consistent with the measured ion temperatures. This

section will describe an electron/ion/impurity coupling calculation which will provide provisional answers these questions.

In the model developed here, collisional coupling between the three different species is assumed to be the only source of power for the ions. Power losses for the majority hydrogenic species will be modeled through charge exchange, and the impurity power loss rate will be modeled phenomenologically through an impurity energy confinement time. The modeling is done at a single point in space; there are no profiles of the parameters.

The rate at which species α gains or loses energy from all other species is determined by the equation[10]

$$\frac{3}{2} n_\alpha \frac{dT_\alpha}{dt} = -\sum_\beta \upsilon^{\alpha/\beta} n_\alpha \left(T_\alpha - T_\beta\right). \tag{3.17}$$

In this equation $\nu^{\alpha/\beta}$ is a collision frequency for temperature equilibration given by

$$n_\alpha \upsilon^{\alpha/\beta} = \frac{4}{\pi} \frac{4\pi n_\alpha n_\beta q_\alpha^2 q_\beta^2 \ln(\Lambda)}{m_\alpha m_\beta v_{T\alpha\beta}^3}, \tag{3.18}$$

$$v_{T\alpha\beta} = \sqrt{\frac{2T_\alpha}{m_\alpha} + \frac{2T_\beta}{m_\beta}}. \tag{3.19}$$

Note that by the symmetry of this expression, we have

$$n_\alpha \frac{dT_\alpha}{dt} = -n_\beta \frac{dT_\beta}{dt}, \tag{3.20}$$

so that the total energy is conserved as it is transferred between species.

To model the evolution of the majority (subscript p) and impurity (subscript i) temperatures, two coupled differential equations are solved:

$$\frac{3}{2} n_p \frac{dT_P}{dt} = -\upsilon^{p/e} n_p \left(T_p - T_e\right) - \upsilon^{p/i} n_p \left(T_p - T_i\right) - \frac{3}{2} n_p T_p n_n < \sigma_{cx} v >, \tag{3.21a}$$

$$\frac{3}{2} n_i \frac{dT_i}{dt} = -\upsilon^{i/e} n_i \left(T_i - T_e\right) - \upsilon^{i/p} n_i \left(T_i - T_p\right) - \frac{\frac{3}{2} n_p T_p n_n}{\tau_{imp}}. \tag{3.21b}$$

In this expression, n_n is the density of neutral hydrogen atoms, τ_{imp} is the confinement time for impurity energy, which is independent of the impurity temperature in this model. The rate coefficient for p+H charge exchange, $<\sigma_{cx}v>$, can be accurately and easily approximated as[11]

$$< \sigma_{cx} v >= 10^{-8} T_p^{.318} (cm^3 / s). \tag{3.23}$$

The equations can be manipulated into their final form as:

$$\frac{dT_P}{dt} = -\frac{2}{3}\upsilon^{p/e}\left(T_p - T_e\right) - \frac{2}{3}\upsilon^{p/i}\left(T_p - T_i\right) - T_p n_n < \sigma_{cx} v >, \tag{3.24a}$$

$$\frac{dT_i}{dt} = -\frac{2}{3}\upsilon^{i/e} n_i \left(T_i - T_e\right) - \frac{2}{3}\upsilon^{i/p} n_i \left(T_i - T_p\right) - \frac{T_p}{\tau_{imp}}. \tag{3.24b}$$

These equations are solved using the ODE23 integrator in Matlab. The electron temperature and the species densities are constants specified before the solution is computed. The equations are written in cgs units, so that charge is in units of statCoulombs, mass in grams, distances in centimeters, energy in ergs, and pressure in ergs/cm^3. Quasineutrality is enforced on the simulations by requiring $n_e=n_p+Z_i n_i$, but the densities are otherwise left as a parameter to be set for each calculation.

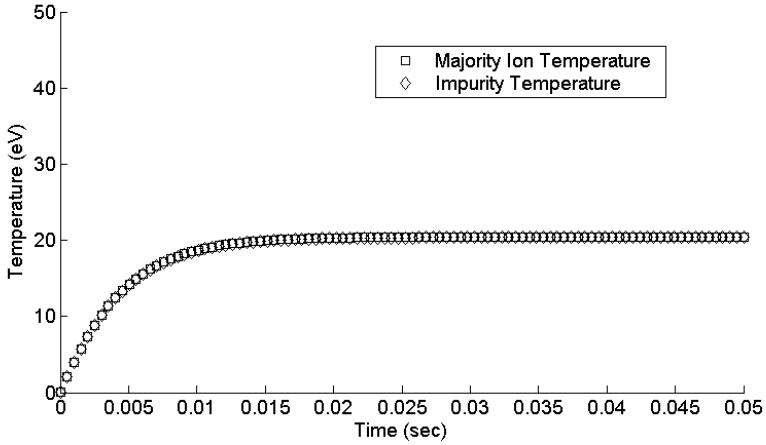

Figure 3.14: Modeled time evolution of the majority and impurity ion temperatures.

An example of this calculation is shown in figure 3.14, for $n_n=7x10^9$, $n_e=5x10^{11}$, and $n_i=1x10^{10}$. The impurity is C^{+4}, with $Z_i=4$, $m_i=12$ amu, and a confinement time $\tau_{imp}=.005$ seconds. The majority and impurity species were started with temperatures of .025eV, while the electron

temperature was set to 200eV. These parameters are approximately appropriate for modeling the HSX plasma. Note that the majority and minority species track each other very closely throughout the entire time evolution. Hence, the impurity species temperature is a good measure of the majority species temperature. Also notice that the temperature reaches a steady state in approximately 10msec, implying that the ion temperature should be quasi-stationary throughout the duration of the measurement (the final 0.035 seconds of an 0.05 second discharge).

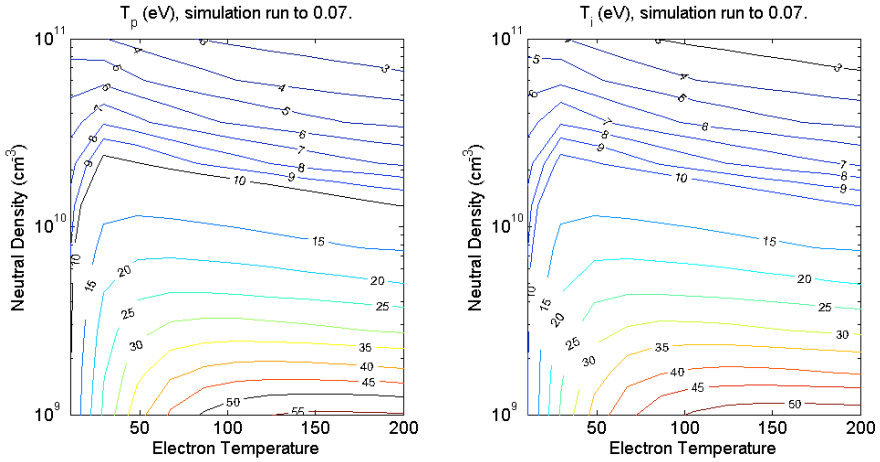

Figure 3.15: Steady state majority (left) and impurity (right) species temperature as a function of the electron temperature and neutral density.

The simulation has been run for many values of the neutral density and electron temperature, with the results shown in figure 3.15. The two contour plots show the majority and impurity species temperatures as functions of the electron temperature and neutral density, at a fixed electron density of 7×10^{11} cm^{-3}. The two ion temperatures track each other very closely over this entire parameter space. The plots show that a neutral density of $\approx 5 \times 10^{9}$ at an electron temperature of ≈100eV implies an ion temperature of 25 eV. These numbers are approximately in keeping with the measurements. An improved model would include profiles and ion heat transport, and would help improve the understanding of these points.

3.4: Determination of the Ion Collisionality

The measured ion temperature allows a determination of the ion collisionality, a point of critical importance in determining the expressions for the viscosity to use. In the highest collisionality regime (Pfirsch-Schlueter), the particles collide faster than they can complete their bounce motion. For a tokamak, the boundary of this regime is given by $\nu > v_{ti}\iota/R$,[12] where R is the major radius of the machine, and ι is the rotational transform. This expression can be made applicable to HSX by simply setting $\iota \rightarrow N - m\iota = 3$. The boundary of the lowest collisionality regime, known as the long mean free path (LMFP) or Galeev-Sagdeev regime, is given by $\nu < \varepsilon_T^{3/2} v_{ti}\iota/R$. This expression can be modified for HSX by simply substituting $\varepsilon_T \rightarrow \varepsilon_H$.

The perpendicular scattering time for ions colliding on electrons was used to calculate the collision frequency. The result of the calculation is shown in figure 3.16, for a surface with $\varepsilon_T = 0.1$. It is clear that for the ion temperatures measured in HSX, the ions are in the plateau collisionality regime.

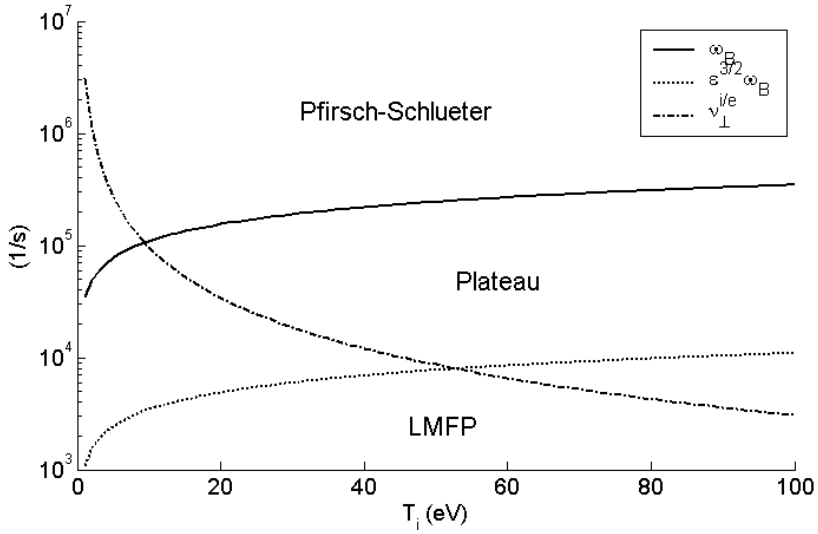

Figure 3.16: Collisionality regime determination as a function of temperature. HSX is in the plateau regime under the conditions described in this dissertation.

3.5 Summary

Two arrays of absolutely calibrated H_α detectors have been installed on HSX. One array is distributed toroidally around the machine at fixed poloidal angle. The second array is at a fixed toroidal angle at the location of the gas puffer. The first array is useful for determining the toroidal asymmetries in hydrogen recycling and neutral density, while the second array is used to determine the hydrogen fueling due to the gas puffer. When coupled to the DEGAS neutral gas code, the system provides a means of estimating the neutral particle distribution in HSX.

Ion Doppler spectroscopy has been performed to measure the temperature of intrinsic impurities in the HSX plasma. The instrument used is a 1 meter Czerny-Turner spectrometer with a CCD detector. Light is coupled to the spectrometer from HSX using a trifurcated fiber bundle. The measured ion temperatures are in the range of 20-25 eV. The impurity ions are strongly collisionally coupled to the majority species ions, so that they are expected to have the same temperature. This temperature is sufficient to place HSX ions in the plateau regime.

[1] J.K. Anderson, PhD. Thesis, U. of Wisconsin-Madison, 2001

[2] Electro-Technical Products, Inc., Model sp200 Spectrum Tube

[3] Optronics Laboratories Series 455 Integrating Sphere

[4] Heifetz, D.B. et. al., J. Comp. Phys. **46,** 309 (1982).

[5] C. Deng, D.L. Brower, W.X.Ding, A.F. Almagri, D.T. Anderson, F.S.B. Anderson, S.P. Gerhardt, P. Probert, and J.N. Talmadge, Rev. Sci. Instrum. **74**, 1625 (2003).

[6] J. Canik, D.T. Anderson, S.P. Gerhardt, and J.N. Talmadge, Proceedings of the 14th Stellarator Workshop, Greifswald, Germany, 2003.

[7] A. Thorne, U. Litzen, and S. Johansson, *Spectrophysics*, (Springer, Berlin, 1999), p. 191.

[8] J.T. Chapman, PhD thesis, U. of Wisconsin-Madison, 1998.

[9] P.R. Bevington and D.K. Robinson, *Data Reduction and Error Analysis for the Physical Sciences*, (McGraw-Hill, Boston, 1992), p. 43.

[10] J.D. Callen, NEEP/Physics/ECE 725 notes, U. of Wisconsin-Madison.

[11] J. Cornelis, R. Sporken, G. Van Oost, and R.R. Weynants, Nuclear Fusion **34**, 171 (1994).

[12] J.D. Callen, NEEP/Physics/ECE 525 notes, U. of Wisconsin-Madison